EUROPEAN ORGANIZATION FOR NUCLEAR RESEARCH

Search for a low mass CP-odd Higgs boson in e^+e^- collisions with the OPAL detector at LEP2

The Opal Collaboration

Abstract

We have analysed the data collected by OPAL at centre-of-mass energies between 189 and 209 GeV searching for Higgs boson candidates from the process $e^+e^- \to h^0Z^0$ followed by the decay of $h^0 \to A^0A^0$ where A^0 is the CP-odd Higgs boson. The search is done in the region where the A^0 mass, m_A, is below the production threshold for $b\bar{b}$, and the CP-even Higgs boson mass m_h is within the range 45–86 GeV/c^2. In this kinematic range, the decay of $h^0 \to A^0A^0$ may be dominant and previous Higgs boson searches have very small sensitivities. This search can be interpreted within any model that predicts the existence of at least one scalar and one pseudoscalar Higgs boson. No excess of events is observed above the expected Standard Model backgrounds. Model-independent limits on the cross-section for the process $e^+e^- \to h^0Z^0$ are derived assuming 100% decays of the h^0 into A^0A^0 and 100% decays of the A^0A^0 into each of the following final states: $c\bar{c}c\bar{c}$, gggg, $\tau^+\tau^-\tau^+\tau^-$, $c\bar{c}$gg, gg$\tau^+\tau^-$ and $c\bar{c}\tau^+\tau^-$. The results are also interpreted in the CP-conserving no-mixing MSSM scenario, where the region $45 \leq m_h \leq 85$ GeV/c^2 and $2 \leq m_A \leq 9.5$ GeV/c^2 is excluded.

G. Abbiendi[2], C. Ainsley[5], P.F. Åkesson[3], G. Alexander[22], J. Allison[16], P. Amaral[9],
G. Anagnostou[1], K.J. Anderson[9], S. Arcelli[2], S. Asai[23], D. Axen[27], G. Azuelos[18,a], I. Bailey[26],
E. Barberio[8], R.J. Barlow[16], R.J. Batley[5], P. Bechtle[25], T. Behnke[25], K.W. Bell[20], P.J. Bell[1],
G. Bella[22], A. Bellerive[6], G. Benelli[4], S. Bethke[32], O. Biebel[31], I.J. Bloodworth[1], O. Boeriu[10],
P. Bock[11], D. Bonacorsi[2], M. Boutemeur[31], S. Braibant[8], L. Brigliadori[2], R.M. Brown[20],
K. Buesser[25], H.J. Burckhart[8], S. Campana[4], R.K. Carnegie[6], B. Caron[28], A.A. Carter[13],
J.R. Carter[5], C.Y. Chang[17], D.G. Charlton[1,b], A. Csilling[8,g], M. Cuffiani[2], S. Dado[21],
G.M. Dallavalle[2], S. Dallison[16], A. De Roeck[8], E.A. De Wolf[8], K. Desch[25], B. Dienes[30],
M. Donkers[6], J. Dubbert[31], E. Duchovni[24], G. Duckeck[31], I.P. Duerdoth[16], E. Elfgren[18],
E. Etzion[22], F. Fabbri[2], L. Feld[10], P. Ferrari[8], F. Fiedler[31], I. Fleck[10], M. Ford[5], A. Frey[8],
A. Fürtjes[8], P. Gagnon[12], J.W. Gary[4], G. Gaycken[25], C. Geich-Gimbel[3], G. Giacomelli[2],
P. Giacomelli[2], M. Giunta[4], J. Goldberg[21], E. Gross[24], J. Grunhaus[22], M. Gruwé[8],
P.O. Günther[3], A. Gupta[9], C. Hajdu[29], M. Hamann[25], G.G. Hanson[4], K. Harder[25],
A. Harel[21], M. Harin-Dirac[4], M. Hauschild[8], J. Hauschildt[25], C.M. Hawkes[1], R. Hawkings[8],
R.J. Hemingway[6], C. Hensel[25], G. Herten[10], R.D. Heuer[25], J.C. Hill[5], K. Hoffman[9],
R.J. Homer[1], D. Horváth[29,c], R. Howard[27], P. Hüntemeyer[25], P. Igo-Kemenes[11], K. Ishii[23],
H. Jeremie[18], P. Jovanovic[1], T.R. Junk[6], N. Kanaya[26], J. Kanzaki[23], G. Karapetian[18],
D. Karlen[6], V. Kartvelishvili[16], K. Kawagoe[23], T. Kawamoto[23], R.K. Keeler[26],
R.G. Kellogg[17], B.W. Kennedy[20], D.H. Kim[19], K. Klein[11], A. Klier[24], S. Kluth[32],
T. Kobayashi[23], M. Kobel[3], S. Komamiya[23], L. Kormos[26], R.V. Kowalewski[26], T. Krämer[25],
T. Kress[4], P. Krieger[6,l], J. von Krogh[11], D. Krop[12], K. Kruger[8], M. Kupper[24],
G.D. Lafferty[16], H. Landsman[21], D. Lanske[14], J.G. Layter[4], A. Leins[31], D. Lellouch[24],
J. Letts[12], L. Levinson[24], J. Lillich[10], S.L. Lloyd[13], F.K. Loebinger[16], J. Lu[27], J. Ludwig[10],
A. Macpherson[28,i], W. Mader[3], S. Marcellini[2], T.E. Marchant[16], A.J. Martin[13], J.P. Martin[18],
G. Masetti[2], T. Mashimo[23], P. Mättig[m], W.J. McDonald[28], J. McKenna[27], T.J. McMahon[1],
R.A. McPherson[26], F. Meijers[8], P. Mendez-Lorenzo[31], W. Menges[25], F.S. Merritt[9], H. Mes[6,a],
A. Michelini[2], S. Mihara[23], G. Mikenberg[24], D.J. Miller[15], S. Moed[21], W. Mohr[10], T. Mori[23],
A. Mutter[10], K. Nagai[13], I. Nakamura[23], H.A. Neal[33], R. Nisius[32], S.W. O'Neale[1], A. Oh[8],
A. Okpara[11], M.J. Oreglia[9], S. Orito[23], C. Pahl[32], G. Pásztor[4,g], J.R. Pater[16], G.N. Patrick[20],
J.E. Pilcher[9], J. Pinfold[28], D.E. Plane[8], B. Poli[2], J. Polok[8], O. Pooth[14], M. Przybycień[8,n],
A. Quadt[3], K. Rabbertz[8], C. Rembser[8], P. Renkel[24], H. Rick[4], J.M. Roney[26], S. Rosati[3],
Y. Rozen[21], K. Runge[10], K. Sachs[6], T. Saeki[23], O. Sahr[31], E.K.G. Sarkisyan[8,j],
A.D. Schaile[31], O. Schaile[31], P. Scharff-Hansen[8], J. Schieck[32], T. Schörner-Sadenius[8],
M. Schröder[8], M. Schumacher[3], C. Schwick[8], W.G. Scott[20], R. Seuster[14,f], T.G. Shears[8,h],
B.C. Shen[4], C.H. Shepherd-Themistocleous[5], P. Sherwood[15], G. Siroli[2], A. Skuja[17],
A.M. Smith[8], R. Sobie[26], S. Söldner-Rembold[10,d], S. Spagnolo[20], F. Spano[9], A. Stahl[3],
K. Stephens[16], D. Strom[19], R. Ströhmer[31], S. Tarem[21], M. Tasevsky[8], R.J. Taylor[15],
R. Teuscher[9], M.A. Thomson[5], E. Torrence[19], D. Toya[23], P. Tran[4], T. Trefzger[31], A. Tricoli[2],
I. Trigger[8], Z. Trócsányi[30,e], E. Tsur[22], M.F. Turner-Watson[1], I. Ueda[23], B. Ujvári[30,e],
B. Vachon[26], C.F. Vollmer[31], P. Vannerem[10], M. Verzocchi[17], H. Voss[8], J. Vossebeld[8,h],
D. Waller[6], C.P. Ward[5], D.R. Ward[5], P.M. Watkins[1], A.T. Watson[1], N.K. Watson[1],
P.S. Wells[8], T. Wengler[8], N. Wermes[3], D. Wetterling[11] G.W. Wilson[16,k], J.A. Wilson[1],
G. Wolf[24], T.R. Wyatt[16], S. Yamashita[23], D. Zer-Zion[4], L. Zivkovic[24]

[1]School of Physics and Astronomy, University of Birmingham, Birmingham B15 2TT, UK
[2]Dipartimento di Fisica dell' Università di Bologna and INFN, I-40126 Bologna, Italy

1

[3]Physikalisches Institut, Universität Bonn, D-53115 Bonn, Germany

[4]Department of Physics, University of California, Riverside CA 92521, USA

[5]Cavendish Laboratory, Cambridge CB3 0HE, UK

[6]Ottawa-Carleton Institute for Physics, Department of Physics, Carleton University, Ottawa, Ontario K1S 5B6, Canada

[8]CERN, European Organisation for Nuclear Research, CH-1211 Geneva 23, Switzerland

[9]Enrico Fermi Institute and Department of Physics, University of Chicago, Chicago IL 60637, USA

[10]Fakultät für Physik, Albert-Ludwigs-Universität Freiburg, D-79104 Freiburg, Germany

[11]Physikalisches Institut, Universität Heidelberg, D-69120 Heidelberg, Germany

[12]Indiana University, Department of Physics, Bloomington IN 47405, USA

[13]Queen Mary and Westfield College, University of London, London E1 4NS, UK

[14]Technische Hochschule Aachen, III Physikalisches Institut, Sommerfeldstrasse 26-28, D-52056 Aachen, Germany

[15]University College London, London WC1E 6BT, UK

[16]Department of Physics, Schuster Laboratory, The University, Manchester M13 9PL, UK

[17]Department of Physics, University of Maryland, College Park, MD 20742, USA

[18]Laboratoire de Physique Nucléaire, Université de Montréal, Montréal, Québec H3C 3J7, Canada

[19]University of Oregon, Department of Physics, Eugene OR 97403, USA

[20]CLRC Rutherford Appleton Laboratory, Chilton, Didcot, Oxfordshire OX11 0QX, UK

[21]Department of Physics, Technion-Israel Institute of Technology, Haifa 32000, Israel

[22]Department of Physics and Astronomy, Tel Aviv University, Tel Aviv 69978, Israel

[23]International Centre for Elementary Particle Physics and Department of Physics, University of Tokyo, Tokyo 113-0033, and Kobe University, Kobe 657-8501, Japan

[24]Particle Physics Department, Weizmann Institute of Science, Rehovot 76100, Israel

[25]Universität Hamburg/DESY, Institut für Experimentalphysik, Notkestrasse 85, D-22607 Hamburg, Germany

[26]University of Victoria, Department of Physics, P O Box 3055, Victoria BC V8W 3P6, Canada

[27]University of British Columbia, Department of Physics, Vancouver BC V6T 1Z1, Canada

[28]University of Alberta, Department of Physics, Edmonton AB T6G 2J1, Canada

[29]Research Institute for Particle and Nuclear Physics, H-1525 Budapest, P O Box 49, Hungary

[30]Institute of Nuclear Research, H-4001 Debrecen, P O Box 51, Hungary

[31]Ludwig-Maximilians-Universität München, Sektion Physik, Am Coulombwall 1, D-85748 Garching, Germany

[32]Max-Planck-Institute für Physik, Föhringer Ring 6, D-80805 München, Germany

[33]Yale University, Department of Physics, New Haven, CT 06520, USA

[a] and at TRIUMF, Vancouver, Canada V6T 2A3

[b] and Royal Society University Research Fellow

[c] and Institute of Nuclear Research, Debrecen, Hungary

[d] and Heisenberg Fellow

[e] and Department of Experimental Physics, Lajos Kossuth University, Debrecen, Hungary

[f] and MPI München

[g] and Research Institute for Particle and Nuclear Physics, Budapest, Hungary

[h] now at University of Liverpool, Dept of Physics, Liverpool L69 3BX, UK

[i] and CERN, EP Div, 1211 Geneva 23

[j] and Universitaire Instelling Antwerpen, Physics Department, B-2610 Antwerpen, Belgium

[k] now at University of Kansas, Dept of Physics and Astronomy, Lawrence, KS 66045, USA

[l] now at University of Toronto, Dept of Physics, Toronto, Canada

[m] current address Bergische Universität, Wuppertal, Germany

[n] and University of Mining and Metallurgy, Cracow, Poland

1 Introduction

The Standard Model (SM) has only one complex doublet of Higgs fields, resulting in one physical mass eigenstate, the neutral Higgs scalar boson [1]. Theoretical limitations of the SM have prompted the development of many other Higgs models. Possible extensions of the SM include the Two Higgs Doublet Models (2HDM). These models predict two complex doublets of scalar fields resulting in five physical Higgs bosons: two neutral CP-even scalars, h^0 and H^0 (with $m_h < m_H$), one CP-odd scalar, A^0, and two charged scalars, $H^\pm$ [2]. The Higgs sector of the Minimal Supersymmetric extension of the Standard Model (MSSM) is of 2HDM(II) type where the introduction of supersymmetry adds new particles and constrains the parameter space of the model. Due to the Higgs boson self-coupling, decays of Higgs bosons into other Higgs bosons become possible if kinematically allowed. In the 2HDM(II), the coupling of the h^0 to $A^0 A^0$ is proportional to:

$$[g\ m_Z/2 \cos(\theta_W)] \cos(2\beta) \sin(\beta + \alpha), \tag{1}$$

where g is the standard SU(2) gauge coupling, m_Z the mass of the Z^0, θ_W is the weak mixing angle, α is the mixing angle that relates the CP-even Higgs states H^0 and h^0 to the field doublets, and $\tan \beta$ is the ratio of the vacuum expectation values of the Higgs scalar fields. When kinematically allowed, the decay $h^0 \to A^0 A^0$ may dominate.

The Standard Model predicts that Higgs bosons accessible at LEP centre-of-mass energies decay preferentially into the heaviest available fermions since the coupling to the Higgs boson is proportional to the fermion mass. This fact has motivated the vast majority of the SM Higgs boson analyses to focus on Higgs boson decays via b quark and τ lepton pairs [3]. OPAL has also performed flavour-independent searches to explore other possibilities [4]. Despite this effort, the region with $m_A < 10$ GeV/c^2 and m_h between 45 and 86 GeV/c^2 remains uncovered within the 2HDM(II) and MSSM parameter scans. The analysis described in this paper is dedicated to a narrow Higgs boson mass region, allowing for the selection of events with very specific kinematics. This guarantees a higher signal detection efficiency while achieving an excellent background rejection. This region has also been investigated by flavour-independent [4] and decay-mode independent [5] analyses but with lower sensitivity.

The properties of the Higgs bosons in the MSSM can be studied in the framework of a constrained model with seven parameters: M_{SUSY}, M_2, μ, $A_{\tilde{q}}$, $\tan \beta$, m_A and $m_{\tilde{g}}$. M_{SUSY} is the sfermion mass and M_2 is the SU(2) gaugino mass parameter, both at the electroweak scale. The parameter μ is the supersymmetric Higgs boson mass parameter, $A_{\tilde{q}}$ is the trilinear Higgs boson-squark coupling parameter, assumed to be the same for up-type squarks and down-type squarks, and $m_{\tilde{g}}$ is the gluino mass. As an example, our results are interpreted in the MSSM no-mixing benchmark scenario [6], which assumes that there is no mixing between the scalar partners of the left-handed and right-handed top quarks, and is determined by the following choice of parameters: $M_{SUSY} = 1$ TeV/c^2, $M_2 = 200$ GeV/c^2, $\mu = -200$ GeV, the stop mixing parameter $X_t \equiv A_{\tilde{q}} - \mu \cot \beta = 0$, $0.4 < \tan \beta < 50$, 4 GeV/$c^2 < m_A <$ 1 TeV/c^2 and $m_{\tilde{g}} = 800$ GeV/c^2. In this scenario, the region for $m_A < 10$ GeV/c^2 and m_h within 45–86 GeV/c^2 is not excluded by the OPAL data, and a smaller mass range with $m_A < 10$ GeV/c^2 and m_h around 70–86 GeV/c^2 also remains unexcluded in the LEP combined data [7]. In this region, the A^0 boson is too light to decay into $b\bar{b}$ and would hence have escaped detection by the analyses using b-tagging. Furthermore, the existing flavour-independent analyses lack the necessary sensitivity to detect or exclude such possibilities.

The region for $m_{\rm h}$ below 45 GeV/c^2 is excluded by LEP 1 [4]. Although this search was originally motivated by the MSSM and 2HDM studies, our results can be extended to any model that predicts the existence of at least one scalar and one pseudoscalar Higgs boson in the mass range of interest and also within models where the physical Higgs bosons are not CP eigenstates, like the CP violating MSSM [8]. For illustrative purposes, we will use the MSSM no-mixing benchmark scenario as a reference in the rest of this paper.

The paper is organized as follows: Section 2 describes the data samples and the OPAL detector. Section 3 gives details of the Monte Carlo simulations and Section 4 describes the event selection. Section 5 covers systematic uncertainties and the results are given in Section 6.

2   Data samples and the OPAL detector

The data used for this analysis were collected during 1998–2000 at LEP in e$^+$e$^-$ collisions at centre-of-mass energies ($E_{\rm CM}$) between 188 and 209 GeV. The data sample is divided into four subsamples, namely $188 \leq E_{\rm CM} \leq 193$ GeV (201.7 pb^{-1}), $193 \leq E_{\rm CM} \leq 198$ (75.1 pb^{-1}), $198 \leq E_{\rm CM} \leq 203.5$ GeV (115.2 pb^{-1}) and $203.5 < E_{\rm CM} \leq 209$ GeV (206.7 pb^{-1}). The analysis is performed separately on each sub-sample and the results are combined. The choice of the subgrouping of centre-of-mass energies is justified by the fact that the production cross-section for the signal does not change appreciably within each of the four subsamples since, for this analysis, we study a region far below the kinematic limit.

The OPAL detector [9] has nearly complete solid angle coverage and hermeticity. The innermost detector of the central tracking is a high-resolution silicon microstrip vertex detector [10] which lies immediately outside of the beam pipe. Its coverage in polar angle[1] is $|\cos\theta| < 0.93$. The silicon microvertex detector is surrounded by a high precision vertex drift chamber, a large volume jet chamber, and z-chambers to measure the z coordinates of tracks, all in a uniform 0.435 T axial magnetic field. The lead-glass electromagnetic calorimeter and the presampler are located outside the magnet coil. In combination with the forward detectors, namely the forward calorimeters, a forward ring of lead-scintillator modules (the "gamma catcher") [9], a forward scintillating tile counter (the "MIP plug") [11], and the silicon-tungsten luminometer [12], the calorimeters provide a geometrical acceptance down to 24 mrad from the beam direction. The silicon-tungsten luminometer measures the integrated luminosity using Bhabha scattering at small angles [13]. The magnet return yoke is instrumented with streamer tubes and thin gap chambers for hadron calorimetry and is surrounded by several layers of muon chambers.

Events are reconstructed from charged particle tracks and energy deposits ("clusters") in the electromagnetic and hadron calorimeters. The tracks and clusters must pass a set of quality requirements similar to those used in previous OPAL Higgs boson searches [14]. In calculating the total visible energies and momenta, $E_{\rm vis}$ and $\vec{P}_{\rm vis}$, of events and individual jets [15], corrections are applied to prevent the double counting of energy of tracks with

---

[1]OPAL uses a right-handed coordinate system where the $+z$ direction is along the electron beam and where $+x$ points to the centre of the LEP ring. The polar angle, θ, is defined with respect to the $+z$ direction and the azimuthal angle, ϕ, with respect to the horizontal, $+x$ direction.

associated clusters [16].

3 Monte Carlo simulation

Monte Carlo samples for signal and background were generated at four different centre-of-mass energies, namely 189, 196, 200 and 206 GeV, chosen to be close to the mean centre-of-mass energy in each data subsample described in Section 2.

We study only h^0Z^0 production since, in the parameter space region of interest for our analysis, its cross-section is about ten times larger than that for h^0A^0 production in the MSSM. The h^0 is forced to decay into two A^0 bosons, $h^0 \to A^0A^0$, and each A^0 can decay into any of the following channels: $c\bar{c}$, $\tau^+\tau^-$ and gg. Resonances are not included in the simulation of A^0 decays. For example, in the MSSM no-mixing scenario, for 3.3 GeV/c$^2 < m_A < 9.5$ GeV/c^2, the A^0 branching fractions into $c\bar{c}$ and $\tau^+\tau^-$ are 0.5-0.9 and 0.4-0.05, depending on the value of $\tan\beta$. Below the $\tau^+\tau^-$ threshold, the A^0 decays nearly exclusively into a gluon pair. Two different Z^0 decay modes are investigated: $Z^0 \to \nu\bar{\nu}$ and $Z^0 \to \ell^+\ell^-$ with $\ell =$e or μ. For each of the Z^0 decay modes, the six final states obtained by all possible combinations of the A^0 decays to gg, $c\bar{c}$ and $\tau^+\tau^-$ have been analysed. In the no-mixing MSSM scenario below the production threshold for $b\bar{b}$, these final states account for between 75% and 100% of the total decays of the A^0 boson [17]. The corresponding Feynman diagram is given in Figure 1.
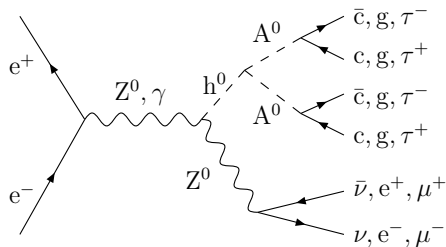
Figure 1: *The Feynman diagram for the processes considered in this analysis.*

Monte Carlo samples were generated with m_A=2, 4, 6, 9 and 11 GeV/c^2 and for $m_h =$ 45, 60, 70, 80, 86 GeV/c^2 at each of the four centre-of-mass energies considered. For each $[m_A,\ m_h]$ combination and each Z^0 decay channel studied, we produced 3000 events for each of the six possible final states using the HZHA2 [18] generator and the full OPAL detector simulation [19].

The branching fraction BR($h^0 \to A^0A^0$) is relatively constant for m_A in the range of 1 to 11 GeV/c^2 for a given value of m_h. The $e^+e^- \to h^0Z^0$ production cross-section does not depend strongly on m_h in the range $45 \leq m_h \leq 86$ GeV/c^2 but increases with increasing $\tan\beta$ values.

Monte Carlo simulations are also used to study the various Standard Model background processes. The 2-fermion events, $e^+e^- \to q\bar{q}$, are simulated with the KK2f generator using

CEEX [20] for the modelling of the initial state radiation and PYTHIA 6.125 [21] for the fragmentation and hadronisation processes. Bhabha events are generated with the BHWIDE [22] and TEEGG [23] generators, $e^+e^- \rightarrow \mu^+\mu^-$ and $e^+e^- \rightarrow \tau^+\tau^-$ events are simulated with the KK2f generator using CEEX and ISR-FSR interference. The 4-fermion samples are generated with grc4f [24] for the $\ell\ell\ell\ell$, $\ell\ell q\bar{q}$, $\ell\nu q\bar{q}$, $\nu\nu q\bar{q}$ and $q\bar{q}q\bar{q}$ channels, where $\ell = e, \mu, \tau$. One 2-photon sample generated at 200 GeV is used for centre-of-mass energies of 189, 196 and 200 GeV and the resulting cross-sections normalised according to the centre-of-mass energy. An independent sample is used at 206 GeV. The various 2-photon processes are modelled by the Vermaseren [25], HERWIG [26], Phojet [27] and F2GEN [28] generators. Typically, at each centre-of-mass energy, the generated 4-fermion and 2-fermion samples are 30 times larger than the data sample, and the 2-photon sample is two to ten times larger than the data.

4 Event selection

In the low A^0 mass region covered by this search the separation between the decay products of the A^0 tends to be small, and they are generally reconstructed as a single jet. The final event topology consists of two jets recoiling against the Z^0 decay products. The invariant mass of a single jet reproduces the mass of the A^0 while the mass of the combined two-jet system reproduces the mass of the h^0. A mass resolution between 0.5 and 3.0 GeV/c^2 is achieved for m_A, while for m_h the resolution is about 8–16 GeV/c^2, all depending on the Z^0 decay mode and the Higgs boson masses.

We perform three separate analyses based on three different Z^0 decay channels: $Z^0 \rightarrow \nu\bar{\nu}$, $\mu^+\mu^-$ and e^+e^-. The event selection criteria are described in detail in the next two sections. After this initial selection, a likelihood variable is constructed for each channel to increase the sensitivity. This likelihood variable is used to perform a scan and set limits.

4.1 The $Z^0 \rightarrow \nu\bar{\nu}$ channel

Events in the process $h^0Z^0 \rightarrow A^0A^0\nu\bar{\nu}$ are characterised by two jets recoiling against an invisible Z^0. Each event is forced into a two-jet topology using the Durham algorithm [15] and a 1-constraint kinematic fit is performed, requiring energy and momentum conservation and forcing the missing mass to be equal to m_Z. Background from cosmic ray events is removed by requiring at least one track per event and applying the two cosmic-ray vetoes described in [29] and [30]. The visible invariant mass is also required to exceed 5 GeV/c^2 to match a corresponding cut used in the generation for the 2-photon MC samples. This cut has no effect on this analysis since it is far from the region of interest for the signal.

The selection criteria used to search for $h^0Z^0 \rightarrow A^0A^0\nu\bar{\nu}$ are mainly based on event shape variables and reconstructed masses. The first four preselection cuts guarantee general data quality, confinement within the detector region and rejection of 2-photon background. The other more specific selection criteria aim mostly at rejecting the other backgrounds. The cuts used are described below:

1. The fraction of total visible energy in the forward detectors must be less than 60%, the event transverse momentum measured w.r.t. the beam axis must exceed 3 GeV and the visible energy of the event must exceed 20% of the centre-of-mass energy.

2. Events are rejected if they have energy deposits exceeding 2 GeV, 5 GeV and 5 GeV in the forward calorimeter, the silicon-tungsten luminometer and the gamma catcher, respectively. This requirement rejects events with initial state radiation or particles escaping detection in the beam pipe.

3. The fraction of good tracks as defined in [14] relative to the total number of tracks should be greater than 0.2.

4. The polar angle, θ, of each jet must satisfy $|\cos\theta| < 0.9$ to reject events with jets partially contained in the detector. This is also a very powerful cut to reduce background contributions from 2-photon and Z/γ^* events with large initial state radiation.

5. The invariant mass of the di-jet system after the kinematic fit must be in the range 30–95 GeV/c^2. This mass should reproduce $m_{\rm h}$ except in the case of $A^0 \to \tau^+\tau^-$ where there are missing neutrinos.

6. The aplanarity[2] must be in the range 0.0002–0.03 and the event shape variable C [31] must be less than 0.8.

7. The polar angle of the missing momentum vector must satisfy $|\cos\theta| < 0.97$.

8. The invariant mass of the more energetic jet must be between 0.5 and 13.0 GeV/c^2. (The mass of the reconstructed jet corresponds to $m_{\rm A}$ within the detector resolution. Since we perform a mass-independent search, we allow for a broad range of values for $m_{\rm A}$.)

9. The invariant mass of the less energetic jet must be between 0.5 and 10.5 GeV/c^2.

The numbers of events passing cuts 1 to 9 are shown in Table 1 for all centre-of-mass energies combined. The numbers of events found in the data are compared to the various backgrounds after each cut. The $q\bar{q}$ and $\ell^+\ell^-$ contributions to the 2-fermion background are listed in two separate columns. The numbers of events expected for a signal hypothesis of $m_{\rm A} = 6$ GeV/c^2 and $m_{\rm h} = 70$ GeV/c^2 in the MSSM no-mixing scenario and the corresponding efficiencies are also shown.

4.1.1 Likelihood selection

A discriminating variable is formed by combining information from the following four variables into a likelihood based on the Projections and Correlations Method [32]:

1. The event shape variable C.

---

[2]The aplanarity is defined as $\frac{3}{2}\lambda_3$, where λ_i are the eigenvalues [$\lambda_1 \geq \lambda_2 \geq \lambda_3$ with $\lambda_1 + \lambda_2 + \lambda_3 = 1$] of the sphericity tensor $S^{\alpha\beta} = \sum_i p_i^\alpha p_i^\beta / \sum_i |\mathbf{p}_i|^2$, and is related to the transverse momentum component out of the event plane.

cut	data	total bgnd	background sources				signal (efficiency)
			q$\bar{\text{q}}$	$\ell^+\ell^-$	4f	2γ	

Z$^0 \to \nu\bar{\nu}$ channel for E_{CM}=189–209 GeV combined							
cut	data	total bgnd	q$\bar{\text{q}}$	$\ell^+\ell^-$	4f	2γ	signal (efficiency)
1	21584	20733.2	9879.4	4265.1	2522.5	4066.3	73.7 (93.2%)
2	13241	12776.5	7793.0	1688.2	2044.5	1250.8	69.2 (87.6%)
3	12990	12597.8	7714.4	1644.2	2012.9	1226.4	68.8 (87.1%)
4	9015	8876.9	5281.1	1300.5	1617.0	678.4	68.8 (87.1%)
5	7837	7809.4	4966.2	1003.1	1332.5	507.6	59.4 (75.2%)
6	5227	5338.8	3991.0	206.0	776.2	365.6	50.9 (64.4%)
7	1571	1547.5	731.8	142.3	585.0	88.4	50.0 (63.3%)
8	854	839.8	429.1	111.1	237.8	61.8	48.6 (61.5%)
9	475	470.5	271.6	57.7	101.6	39.6	47.7 (60.4%)
$\mathcal{L} > 0.88$	18	14.9	0.1	1.0	13.8	0.0	38.0 (48.1%)

Table 1: *The numbers of observed events together with the Monte Carlo expectation for the various sources of background given for the combined sample ($189 \leq E_{\text{CM}} \leq 209$ GeV) for the Z$^0 \to \nu\bar{\nu}$ channel. The corresponding efficiencies are given within parentheses for one signal hypothesis ($m_A = 6$ GeV/c^2, $m_h = 70$ GeV/c^2) in the MSSM no-mixing scenario. The various cuts are described in the text. The likelihood cut is only given for illustrative purposes. It is not used to set the limits in Section 6.*

2. The acoplanarity[3] angle of the two jets.

3. The invariant mass of the more energetic jet.

4. The invariant mass of the less energetic jet.

These variables are shown for the data, the different sources of background and the reference signal in Figure 2 after all preselection cuts given in Section 4.1 are applied and for all centre-of-mass energies combined. To form the reference distributions for the signal, the distributions for sixteen [m_A,m_h] mass hypotheses obtained for m_h= 60, 70, 80, 86 GeV/c^2 and m_A= 2, 4, 6, 9 GeV/c^2 are summed after relative re-normalization according to the integrated luminosity of the data and their production cross-section. For the background, three reference distributions are used: the $\ell^+\ell^-$, the 4-fermion, and the combined 2-photon and q$\bar{\text{q}}$ samples. Hence, the data are compared to four reference distributions: three for the Standard Model background and one single distribution for the signal. The likelihood function used to derive our result is formed separately for each centre-of-mass energy considered. The distribution of the likelihood input variables for all centre-of-mass energies combined is shown in Figure 2 for illustrative purposes only. The efficiencies for each mass hypothesis are also determined separately at each of the [m_A,m_h] mass hypotheses and for each centre-of-mass energy. A small correction has to be applied to the efficiencies and backgrounds due

---

[3]The acoplanarity angle is the absolute value of 180° minus the opening angle between the two jets in the plane transverse to the beam direction.

to accelerator-related backgrounds in the forward detectors which are not simulated. From random beam crossing events the correction factors have been evaluated to be 3.1%, 3.6%, 3.6% and 3.2% for $\sqrt{s} = 189$, 196, 200 and 206 GeV, respectively.

For illustrative purposes, a cut at 0.88 placed on the likelihood variable would reject most background events and retain sufficient efficiency at all mass hypotheses considered. The same cut would be used for all data sets and is chosen by maximising the signal purity times the efficiency of our signal reference at all energies. After this cut, 18 events would be retained in data compared to 14.9 expected from SM backgrounds. The likelihood distribution function is shown in Figure 5 (a) for the data, the Standard Model backgrounds and the reference signal for the 189–209 GeV data combined. The likelihood cut is not used to set limits in Section 6. The signal efficiency ranges from 38% to 75% for $m_A = 6$ GeV/c^2(see Figure 6(a)). It drops down between 21% and 53% for $m_A = 11$ GeV/c^2.

4.2 The $Z^0 \rightarrow \mu^+\mu^-$ and $Z^0 \rightarrow e^+e^-$ channels

The leptonic Z^0 channels, namely $h^0Z^0 \rightarrow A^0A^0e^+e^-$ and $h^0Z^0 \rightarrow A^0A^0\mu^+\mu^-$ are also investigated. These events are characterised by the presence of two jets with invariant mass compatible with the h^0 mass and a lepton pair with invariant mass close to the Z^0 mass.

The electron and muon analyses share the first three preselection cuts listed below. The selection starts with lepton identification. First the event is required to have one isolated lepton in association with two jets by applying the same selection criteria used in [33] for the isolation and identification of a lepton in qq$\ell\nu$ events from W^+W^- decays. The selection is based on the probability for a track to be correctly associated with an isolated lepton. The probability is obtained with a likelihood method based on kinematic and lepton identification variables. No requirement on the number of tracks is made to avoid biasing the selection against low multiplicity events. Then the identification of two isolated leptons with the same flavour and opposite charge produced in association with two jets is required and the selected events are forced into a two jet configuration using the Durham algorithm without including the two best lepton candidates.

The next two cuts are applied to ensure confinement within the detector while the remaining selection criteria are optimised for background rejection and differ for the two analyses. This was necessary in order to reduce the large 2-photon background contribution in the electron channel. All cuts are optimised to maximise purity times efficiency for a mixture of all signal hypotheses.

1. The isolation and identification of two oppositely charged leptons (e^+e^- or $\mu^+\mu^-$) in association with two jets.

2. To avoid events having particles lost in the beampipe, both jets must have $|\cos\theta| < 0.99$.

3. The visible energy must be greater than 0.78 of the centre-of-mass energy. This cut ensures the event is well-contained within the detector and rejects some of the 4-fermion background.

Muon channel

4a. The invariant mass of the more energetic jet is required to be less than 25 GeV/c^2.

5a. The invariant mass of the less energetic jet has to be less than 15 GeV/c^2.

Electron channel

4b. The invariant mass of the two leptons should be between 66 and 115 GeV/c^2.

5b. The number of charged tracks in each jet should be less than 10. This cut drastically reduces the 4-fermion background.

6b. The invariant mass of the more energetic jet is required to be less than 36 GeV/c^2.

7b. The invariant mass of the less energetic jet must be less than 30 GeV/c^2.

8b. The angle between the two jets must exceed 1.6 rad to reduce the 2-photon background.

muon channel for E_{CM}=189–209 GeV combined						
cut	data	total	background sources			signal
		bgnd	2f	4f	2γ	(efficiency)
1	56	61.0	0.7	60.0	0.1	10.1 (77.4%)
2	55	60.0	0.6	59.4	0.0	10.1 (77.4%)
3	44	47.4	0.2	47.2	0.0	9.5 (72.8%)
4a	33	37.6	0.0	37.6	0.0	9.1 (69.8%)
5a	27	30.5	0.0	30.5	0.0	8.8 (67.5%)
$\mathcal{L} > 0.56$	4	3.6	0.0	3.6	0.0	7.8 (59.8%)

Table 2: *The numbers of observed events together with the Monte Carlo expectation for the various sources of background given for the combined sample ($189 \leq E_{CM} \leq 209$ GeV) for the muon channel. The corresponding efficiencies are given within parentheses for one signal hypothesis ($m_A = 6$ GeV/c^2, $m_h = 70$ GeV/c^2) in the MSSM no-mixing scenario. The various cuts are described in the text. The 2-fermion sample contains both q$\bar{q}$ and $\ell^+\ell^-$ events. The likelihood cut is only given for illustrative purposes and is not used to set the limits in Section 6.*

The number of events passing each of these cuts can be found in Tables 2 and 3 for the muon and electron channels, respectively. The numbers of events selected in the data are compared with the total background expected from the 4-fermion, 2-fermion and 2-photon samples after each cut. The number of events expected for a signal hypothesis of $m_h = 70$ GeV/c^2 and $m_A = 6$ GeV/c^2 in the MSSM no-mixing scenario is also shown. The 2-fermion background consists of q$\bar{q}$ and $\tau^+\tau^-$ events, but only q$\bar{q}$ events survive the preselection. While in the $Z^0 \rightarrow \mu^+\mu^-$ channel the two-photon background is fully rejected by the preselection, in

11

electron channel for E_{CM}=189–209 GeV combined						
cut	data	total	background sources			signal
		bgnd	2f	4f	2γ	(efficiency)
1	100	103.6	1.9	80.4	21.1	9.9 (75.9%)
2	99	99.5	1.8	79.3	18.5	9.7 (74.4%)
3	77	79.5	1.4	62.0	16.1	9.2 (70.6%)
4b	35	35.9	0.4	29.5	6.1	7.4 (56.7%)
5b	23	19.7	0.2	15.2	4.3	7.1 (54.4%)
6b	21	17.8	0.1	14.1	3.5	6.3 (48.3%)
7b	20	16.2	0.1	13.1	2.8	6.1 (46.8%)
8b	19	14.3	0.1	12.3	1.8	6.0(46.0%)
$\mathcal{L} > 0.52$	4	3.6	0.0	2.5	1.1	5.1 (39.1%)

Table 3: *The numbers of observed events together with the Monte Carlo expectation for the various sources of background given for the combined sample ($189 \leq E_{CM} \leq 209$ GeV) for the electron channel. The corresponding efficiencies are given within parentheses for one signal hypothesis ($m_A = 6$ GeV/c^2, $m_h = 70$ GeV/c^2) in the MSSM no-mixing scenario. The various cuts are described in the text. The 2-fermion sample contains both q$\bar{q}$ and $\ell^+\ell^-$ events. The likelihood cut is only given for illustrative purposes and is not used to set the limits in Section 6.*

the $Z^0 \to e^+e^-$ channel some hadronic tagged two-photon events[4] survive the preselection cuts. To decrease the large statistical error on this background, all Monte Carlo generated 2-photon events have been used at each centre-of-mass energy.

4.2.1 Likelihood selection

A discriminating variable is formed as for the $Z^0 \to \nu\bar{\nu}$ channel by combining information from the variables listed below into a likelihood based on the Projections and Correlations method [32]. The sixteen signal hypotheses obtained for m_h= 60, 70, 80, 86 GeV/c^2 and m_A= 2, 4, 6, 9 GeV/c^2 are combined to form one single reference signal distribution for each input variable as described in Section 4.1.1. This is done separately for the two leptonic channels. The variables used as inputs for the two likelihood functions are described here:

---

[4]Two-photon events in which one or both scattered electrons are detected [34].

Muon channel

1. Angle between the more energetic muon and the nearest jet.

2. Angle between the less energetic muon and the nearest jet.

3. Reconstructed invariant mass of the more energetic jet.

4. Reconstructed invariant mass of the less energetic jet.

Electron channel

1. Invariant mass of the electron pair.

2. Angle between the less energetic electron and the nearest jet.

3. Reconstructed invariant mass of the more energetic jet.

4. Reconstructed invariant mass of the less energetic jet.

5. Angle between the two jets.

The distributions of the input variables for the data, the total background and the reference signal after applying all preselection cuts are shown in Figures 3 and 4 for the muon and electron channels, respectively. For the background, only one reference distribution is used in both channels consisting of the 4-fermion background sample: too few 2-photon and 2-fermion events survive the preselection in the electron channel to use them as reference histograms. The likelihood distribution function is shown for the data, the Standard Model backgrounds and the reference signal in Figures 5 (b) and (c) for the muon and electron analyses, respectively.

For illustrative purposes, a cut on the likelihood value could be set at 0.56 for the muon and 0.52 for the electron analysis to optimise background rejection and signal detection efficiency at all mass hypotheses considered by maximising the purity times signal efficiency of our signal reference. This cut would retain four events in data compared to 3.6 expected from SM backgrounds both in the muon and electron channels. This cut is not used to set limits in Section 6. For the muon channel, the signal efficiency ranges from 32% to 77% for $m_A = 6$ GeV/c^2 (see Figure 6(c)) and between 29% and 75% for $m_A = 11$ GeV/c^2. For the electron channel, the signal efficiency ranges between 14 and 57% at $m_A = 6$ GeV/c^2 (see Figure 6(e)) and between 4 and 46% at $m_A = 11$ GeV/c^2.

5   Systematic uncertainties

Many effects related to possible inadequacies in the simulation of physical quantities in the Monte Carlo samples contribute to the systematic uncertainty. These contributions are listed in Table 4 for the $Z^0 \to \nu\bar{\nu}$, $Z^0 \to \mu^+\mu^-$ and $Z^0 \to e^+e^-$ channels. They are added in quadrature to obtain the total systematic uncertainty for each channel. The evaluation of each source considered is described here:

	$Z^0 \to \nu\bar{\nu}$ channel		$Z^0 \to \mu^+\mu^-$ channel		$Z^0 \to e^+e^-$ channel	
source	bgnd	signal	bgnd	signal	bgnd	signal
$\tan\lambda$	±0.1	±(0.0 − 1.3)	±0.3	±(0.0 − 1.6)	±0.4	±(0.0 − 0.7)
κ	±0.2	±(0.1 − 1.1)	±1.2	±(0.2 − 7.0)	±2.7	±(0.3 − 2.2)
inputs to $\mathcal{L}$	±8.0	±(0.7 − 8.3)	±8.9	±(1.0 − 4.2)	±10.2	±(2.0 − 8.3)
SM cross-sec.	±2.0	–	±2.0	–	±6.7	–
MC statistics	±4.8	±(1.4 − 13.5)	±10.0	±(1.4 − 11.9)	±11.7	±(2.0 − 10.5)
lepton ID	–	–	±0.9	±0.9	±2.3	±2.3
total	±9.8	±(1.7 − 15.9)	±13.6	±(2.2 − 14.5)	±17.3	±(4.4 − 13.7)

Table 4: *Contributions to the systematic uncertainties for the $Z^0 \to \nu\bar{\nu}$, $Z^0 \to \mu^+\mu^-$ and $Z^0 \to e^+e^-$ channels expressed in percent for the signal Monte Carlo and the Standard Model background, as described in the text. The error on the signal corresponds to the range of values obtained for the generated $[m_A, m_h]$ values for MSSM Higgs bosons in the no-mixing scenario.*

- **Simulation of likelihood input variables**. Each likelihood input variable is re-scaled in the Monte Carlo so as to reproduce the mean and variance of the distribution seen in data. This scaling is done at the level of the preselection cuts described in Sections 4.1 and 4.2. After the illustrative likelihood cut, the difference in the number of selected background events and signal efficiencies before and after re-scaling is used to derive the systematic uncertainty. The observed variations are then added in quadrature.

- **Detector tracking resolution**. The tracking parameters for all Monte Carlo samples are smeared, varying the resolution by ±10% in $\tan\lambda$ and ±6% in κ separately to evaluate their contributions to the track reconstruction. Here, $\tan\lambda = \cot\theta$, where θ is the track polar angle and κ is the track curvature at the point of closest approach to the origin. The variation sizes are based on a comparison between data and Monte Carlo using muon pairs and Bhabha events.

- **Background cross-section determination**. The overall 4-fermion cross-section uncertainty is assumed to be about ±2% [35], reflecting differences in calculations of the W^+W^- and Z^0Z^0 cross-sections when comparing results from various generators. The same error is assigned to 2-fermion Standard Model background. For the electron channel a 20% error on the cross-section for tagged hadronic two-photon events is assumed based on a recent OPAL measurement [36].

- **Lepton identification.** Lepton identification is performed as in [33]. Systematic errors are assigned to account for observed differences between data and Monte Carlo simulation in lepton identification and tracking efficiency. The lepton identification mismodelling is studied using "mixed events". These events are formed by combining two kinds of events recorded at $\sqrt{s} = 91$ GeV: a $Z^0 \to q\bar{q}$ event is combined with half of a $Z^0 \to \ell^+\ell^-$ event to simulate a $W^+W^- \to qq\ell\nu$ event. The systematic error is obtained by comparing data and Monte Carlo lepton identification efficiency in

mixed events and is estimated to be 0.29% for electrons and 0.24% for muons. The second contribution to the uncertainty accounts for tracking losses. To determine this contribution, $Z^0 \to e^+e^-$ and $Z^0 \to \mu^+\mu^-$ events in data recorded at $\sqrt{s} = 91$ GeV are compared to Monte Carlo events. The difference in the tracking efficiency is used to extract a 1.1% systematic error for electrons and a 0.4% error for muons. These two contributions are added in quadrature for each lepton, then doubled since our selection requires two such leptons per event, leading to a systematic uncertainty of 2.3% for electrons and 0.9% for muons.

- **Monte Carlo statistics**. The numbers of events passing the preselection as well as the size of the Monte Carlo sample before preselection are used to determine the contribution from statistically limited samples based on binomial statistics. Table 4 gives the contributions at $\sqrt{s} = 189$ GeV. In the limit calculation the systematic errors for each different final state and centre-of-mass energy are used.

To illustrate the effect of the systematic uncertainties after the illustrative likelihood cut described in Sections 4.1.1 and 4.2.1, a signal hypothesis of $m_A = 6$ GeV/c^2 and $m_h = 70$ GeV/c^2 would contribute 38.0 ± 0.8 events in addition to the 14.9 ± 1.5 events expected from Standard Model backgrounds in the $Z^0 \to \nu\bar{\nu}$ channel after combining all Monte Carlo samples at 189, 196, 200 and 206 GeV. For the combined leptonic channels, the signal would contribute 12.9 ± 0.4 events in addition to the 7.2 ± 1.1 expected events from backgrounds. There are 18 candidates selected in the data for the invisible channel and eight candidates in the leptonic channels as shown in Tables 1, 2 and 3.

6 Results

The analyses presented here are designed to explore the possibilities of a low mass Higgs boson, namely for m_A below the $b\bar{b}$ threshold. No significant excess of events is observed in either the invisible or leptonic Z^0 decay modes. Hence we set limits within two different scenarios: a model-independent scenario and the MSSM no-mixing benchmark parameter scenario. We obtain 95% confidence level (CL) exclusion limits using standard statistical procedures based on the likelihood ratio technique [37] as applied in other OPAL publications. The likelihood variables described in Sections 4.1.1 and 4.2.1 are used as discriminating variables for the limit calculation without cutting on this variable. For the signal, the likelihood variable and the efficiency are calculated for each centre-of-mass energy, each $[m_A,m_h]$ hypothesis and each final state. The search efficiency is computed from Monte Carlo samples produced for each A^0 pair decay channel (namely $A^0A^0 \to c\bar{c}c\bar{c}$, $\tau^+\tau^-\tau^+\tau^-$, gggg, $c\bar{c}\tau^+\tau^-$, $c\bar{c}gg$, $\tau^+\tau^-gg$), each $[m_A, m_h]$ hypothesis and each centre-of-mass energy considered in this study. For the m_A and m_h points located between the mass points where Monte Carlo samples were generated, the efficiencies, the shape of the likelihood distribution and the systematic errors are interpolated using a weighted mean of the relevant quantity for the four nearest $[m_A, m_h]$ mass points. The likelihood variable for backgrounds and data are determined separately for each centre-of-mass energy. The efficiencies are shown in Figure 6 at $E_{CM} = 189$ GeV for each A^0A^0 decay channel versus m_A and m_h, both for the missing energy and the leptonic analyses. Similar behaviour is observed for any other choice of the masses and centre-of-mass energy. The efficiencies are calculated neglecting cases where the

A^0 would decay to resonances. The search is still sensitive to the A^0 decays to resonances since the resonant states decay preferentially into gg, $\tau^+\tau^-$ and c$\bar{c}$ [38].

6.1 Model-independent limits

We calculate limits on the cross-section for the process $e^+e^- \rightarrow h^0Z^0$. The limits can be extracted in terms of a scale factor s^2 that relates the cross-section for the production of h^0Z^0, in any specific theoretical interpretation of our experimental search, to the Standard Model cross-sections:

$$\sigma_{h^0Z^0} = s^2 \sigma_{H^0_{SM}Z^0}. \tag{2}$$

The $h^0 \rightarrow A^0A^0$ branching ratio is assumed to be 100%. The limits are extracted for 100% branching ratio of A^0A^0 into c$\bar{c}$c$\bar{c}$, gggg, $\tau^+\tau^-\tau^+\tau^-$, c$\bar{c}$gg, gg$\tau^+\tau^-$ and c$\bar{c}\tau^+\tau^-$. For each of the six final states studied, Figure 7 shows the iso-contours of 95% CL exclusion for s^2 in the m_A and m_h mass plane with $2 \leq m_A \leq 11$ GeV/c^2 and 45 GeV/$c^2 \leq m_h \leq$ 86 GeV/c^2. The scan is performed in 1 GeV/c^2 steps in m_h and in 0.5 GeV/c^2 steps in m_A. The $\tau^+\tau^-\tau^+\tau^-$ channel has the largest exclusion power despite the fact that the selection efficiency is slightly lower than in the other decay channels since the signal is better separated from the background.

6.2 MSSM no-mixing scenario interpretation

We scan the region with $2 \leq m_A \leq 11$ GeV/c^2 and 45 GeV/$c^2 \leq m_h \leq 85$ GeV/c^2 in the m_A versus m_h plane for the MSSM benchmark parameter scenario. The maximum theoretically allowed value for m_h in this scenario is 85 GeV/c^2 [6]. The scan procedure is the same as that of the OPAL MSSM parameter scan [39]. The expected number of events for the signal is adjusted so as to correspond to specific production cross-section and branching ratios for a particular point of the parameter space. The 95% CL expected and observed exclusion regions are shown in Figure 8. The region for $45 \leq m_h \leq 82$ GeV/c^2 is excluded for $2 \leq m_A \leq 9.85$ GeV/c^2, i.e., up to the b$\bar{b}$ threshold where $A^0 \rightarrow$ b$\bar{b}$ decays become dominant. For $82 \leq m_h \leq 85$ GeV/c^2, the region is excluded for $2 \leq m_A \leq 9.5$ GeV/c^2. The whole region below the b$\bar{b}$ threshold was expected to be excluded but is not due to the presence of candidates in the missing energy channel (see the third bin from the right in Figure 5 (a)).

7 Conclusions

We have searched for the process $e^+e^- \rightarrow h^0Z^0$ with Z^0 decaying into $\nu\bar{\nu}$, e^+e^-, $\mu^+\mu^-$ and h^0 decaying into A^0A^0 with m_A below the b$\bar{b}$ threshold. Six different decay modes for the A^0A^0 system have been investigated: c$\bar{c}$c$\bar{c}$, gggg, $\tau^+\tau^-\tau^+\tau^-$, c$\bar{c}$gg, gg$\tau^+\tau^-$ and c$\bar{c}\tau^+\tau^-$. No evidence for the presence of a signal has been found and exclusion limits have been derived both in a model-independent way and within the MSSM no-mixing benchmark scenario.

Large areas of the parameter space investigated have been excluded. In particular, in the MSSM no-mixing scenario, the whole rectangular area for $2 \leq m_A \leq 9.5$ GeV/c^2 and $45 \leq m_h \leq 85$ GeV/c^2 is excluded at 95% CL, while the expected exclusion area is $2 \leq m_A \leq 9.8$ GeV/c^2 and $45 \leq m_h \leq 85$ GeV/c^2. These limits are the best obtained so far in this region of parameter space, which has not previously been excluded.

References

[1] P.W. Higgs, Phys. Lett. **12** (1964) 132;
F. Englert and R. Brout, Phys. Rev. Lett. **13** (1964) 321;
G.S. Guralnik, C.R. Hagen, and T.W.B. Kibble, Phys. Rev. Lett. **13** (1964) 585.

[2] J.F. Gunion, H.E. Haber, G.L. Kane and S. Dawson, *The Higgs Hunter's Guide*, Perseus Publishing, Cambridge, Massachusetts, 2000.

[3] ALEPH Collaboration, A. Heister *et al.*, Phys. Lett. **B526** (2002) 191;
DELPHI Collaboration, P. Abreu *et al.*, Phys. Lett. **B499** (2001) 23;
L3 Collaboration, M.Acciarri *et al.*, Phys. Lett. **B495** (2001) 18;
OPAL Collaboration, G. Abbiendi *et al.*, Phys. Lett. **B499** (2001) 38.

[4] OPAL Collaboration, G. Abbiendi *et al.*, Eur. Phys. J. **C18** (2001) 425.

[5] *Decay-mode independent searches for new scalar bosons with the OPAL detector at LEP*, OPAL Collaboration, G. Abbiendi *et al.*, CERN-EP-2002-032, submitted to Eur. Phys. J. C.

[6] *Suggestions for Improved Benchmark Scenarios for Higgs-Boson Searches at LEP2*, M.S. Carena, S. Heinemeyer, C.E.M. Wagner and G. Weiglein, hep-ph/9912223.

[7] D. Zer-Zion, *Beyond the Standard Model Higgs searches at LEP (Part A)*, Proceedings of the International Europhysics Conference on High Energy Physics, July 2001, Budapest, Hungary. J.H.E.P., PRHEP-hep2001/144, `http://www.hep2001.elte.hu/`

[8] M. Carena, J. R. Ellis, A. Pilaftsis and C. E. Wagner, Phys. Lett. **B495** (2000) 155.

[9] OPAL Collaboration, K. Ahmet *et al.*, Nucl. Instr. and Meth. **A305** (1991) 275.

[10] S. Anderson *et al.*, Nucl. Instr. and Meth. **A403** (1998) 326.

[11] G. Aguillion *et al.*, Nucl. Instr. and Meth. **A417** (1998) 266.

[12] B.E. Anderson *et al.*, IEEE Transactions on Nuclear Science **41** (1994) 845.

[13] OPAL Collaboration, K. Ackerstaff *et al.*, Phys. Lett. **B391** (1997) 221.

[14] OPAL Collaboration, R. Akers *et al.*, Phys. Lett. **B327** (1994) 397.

[15] N. Brown and W.J. Stirling, Phys. Lett., **B252** (1990) 657;
S. Catani *et al.*, Phys. Lett., **B269** (1991) 432;
S. Bethke, Z. Kunszt, D. Soper and W.J. Stirling, Nucl. Phys., **B370** (1992) 310;
N. Brown and W.J. Stirling, Z. Phys., **C53** (1992) 629.

[16] OPAL Collaboration, K. Ackerstaff *et al.*, Eur. Phys. J. **C2** (1998) 213.

[17] S. Heinemeyer, W. Hollik and G. Weiglein, Comput. Phys. Commun. **124** (2000) 76;
S. Heinemeyer, W. Hollik and G. Weiglein, *Feynhiggs and Feynhiggsfast: Programs for higher order calculations in the neutral CP even Higgs boson sector of the MSSM*, LC-TH-2001-065.

[18] P. Janot *et al.*, *Workshop on Physics at LEP2*, CERN 96-01, Vol. 2, 309.
For HZHA2, see `http://alephwww.cern.ch/∼janot/Generators.html`.

[19] J. Allison *et al.*, Nucl. Instr. and Meth. A**317** (1992) 47.

[20] S. Jadach, B.F. Ward and Z. Was, Phys. Lett. **B449** (1999) 97.

[21] T. Sjöstrand, Comp. Phys. Comm. **82** (1994) 74;
T. Sjöstrand, LU TP 95-20.

[22] S. Jadach, W. Placzek and B.F.L. Ward, Phys. Lett., **B390** (1997) 298.

[23] D. Karlen, Nucl. Phys. **B289** (1987) 23.

[24] J. Fujimoto *et al.*, Comp. Phys. Comm. **100** (1997) 128;
J. Fujimoto *et al.*, *Workshop on Physics at LEP2*, CERN 96-01, Vol. 2, 30.

[25] J. A. M. Vermaseren, Nucl. Phys. **B229** (1983) 347;
R. Bhattacharya, G. Grammer Jr. and J. Smith, Phys. Rev. **D15** (1977) 3267;
J. Smith, J.A.M. Vermaseren and G. Grammer Jr., Phys. Rev. **D15** (1977) 3280;
J. A. M. Vermaseren, J. Smith and G. Grammer Jr., Phys. Rev. **D19** (1979) 137.

[26] G. Marchesini *et al.*, Comp. Phys. Comm. **67** (1992) 465.

[27] R. Engel, Z. Phys. **C66** (1995) 203;
R. Engel, J. Ranft, Phys. Rev. **D54** (1996) 4246.

[28] A. Buijus *et al.*, Comp. Phys. Comm. **79** (1994) 523.

[29] OPAL Collaboration, R. Akers *et al.* Z. Phys. **C61** (1994) 19.

[30] OPAL Collaboration, G. Abbiendi *et al.*, Eur. Phys. J. **C8** (1999) 23.

[31] G. Hanson *et al.*, Phys. Rev. Lett. **35** (1975) 1609;
G. Parisi, Phys. Lett., **B74** (1978) 65.

[32] D. Karlen, Computers in Physics, 12:4 (1998) 380.

[33] OPAL Collaboration, K. Ackerstaff *et al.*, Eur. Phys. J. **C1** (1998) 395.

[34] P. Aurenche and G.A. Schuler, *Workshop on Physics at LEP2*, CERN 96-01, Vol. 1, 293.

[35] M.W. Grünewald, G. Passarino et al "Four-fermion Production in electron positron collisions", hep-ph/0005309

[36] OPAL Collaboration, G. Abbiendi *et al.*, Phys. Lett. **B533** (2002) 207.

[37] T. Junk, Nucl. Instr. Meth. **A434** (1999) 435.

[38] M. Drees and K.-I. Hikasa, Phys. Rev. **D41** (1990) 1547.

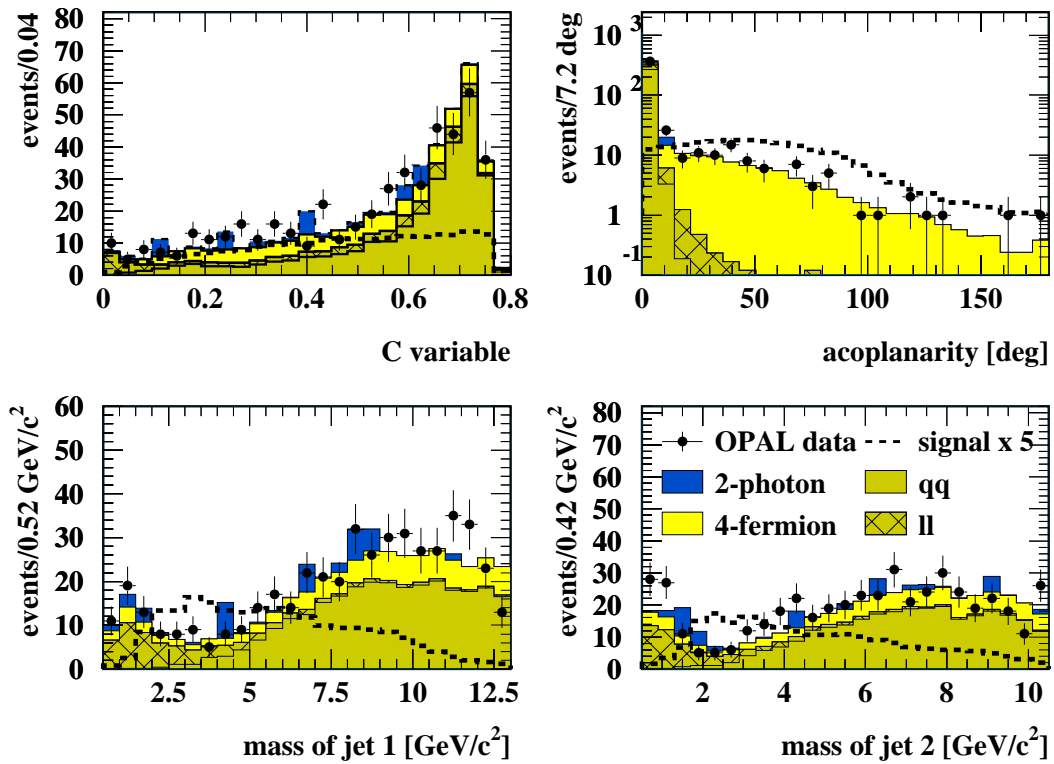[39] OPAL Collaboration, G. Abbiendi *et al.*, Eur. Phys. J. **C12** (2000) 567.

Figure 2: *The four input variables used for the likelihood function of the* $Z^0 \rightarrow \nu\bar{\nu}$ *channel after all preselection cuts are applied. The contributions from the Standard Model backgrounds are added and normalised to the data integrated luminosity. The results are shown here for* E_{CM}*=189–209 GeV combined. The contribution from the reference signal is scaled up by a factor of five.*
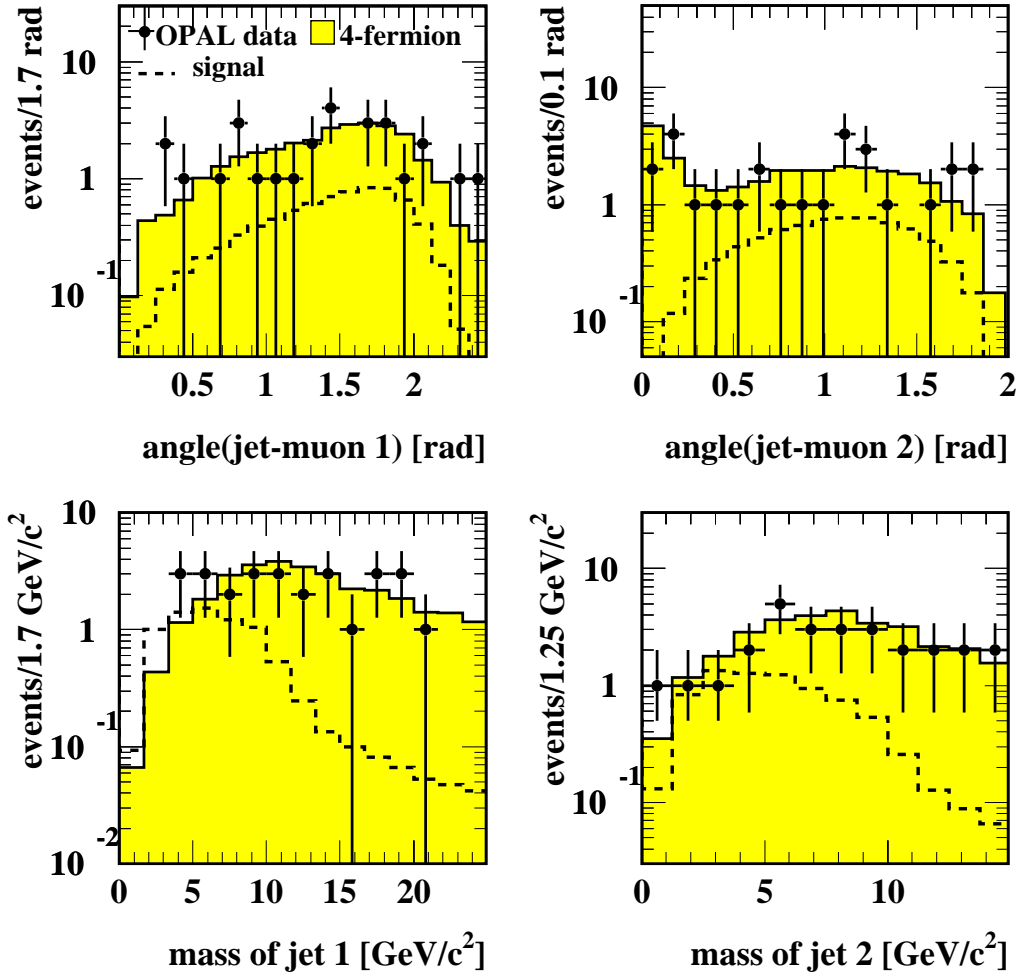
Figure 3: *The four input variables used for the likelihood function in the muon channel after all preselection cuts for E_{CM}=189–209 GeV/c^2 combined, where the labels 1 and 2 refer to the more and less energetic muon and jet, respectively. The only contribution from Standard Model backgrounds surviving the preselection, namely the 4-fermion sample, is compared to the data. The contribution from the reference signal is also shown.*
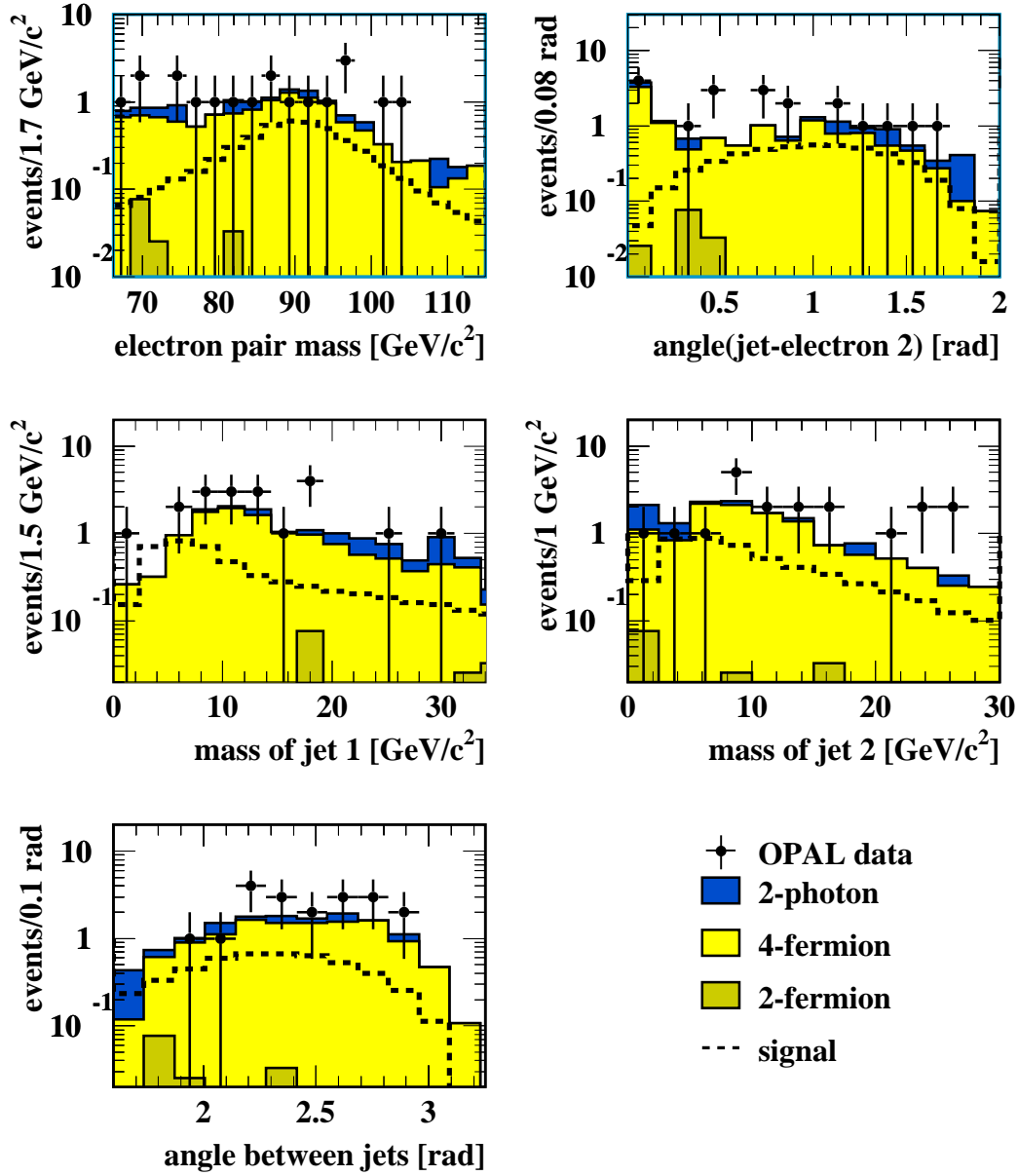
Figure 4: *The five input variables used for the likelihood function after all preselection cuts in the electron channel for E_{CM}=189–209 GeV combined, where the labels 1 and 2 refer to the more and less energetic electron and jet, respectively. The contributions of Standard Model backgrounds surviving the preselection, namely the 4-fermion, 2-fermion and 2-photon samples, are compared to the data. The contribution from the reference signal is also shown.*
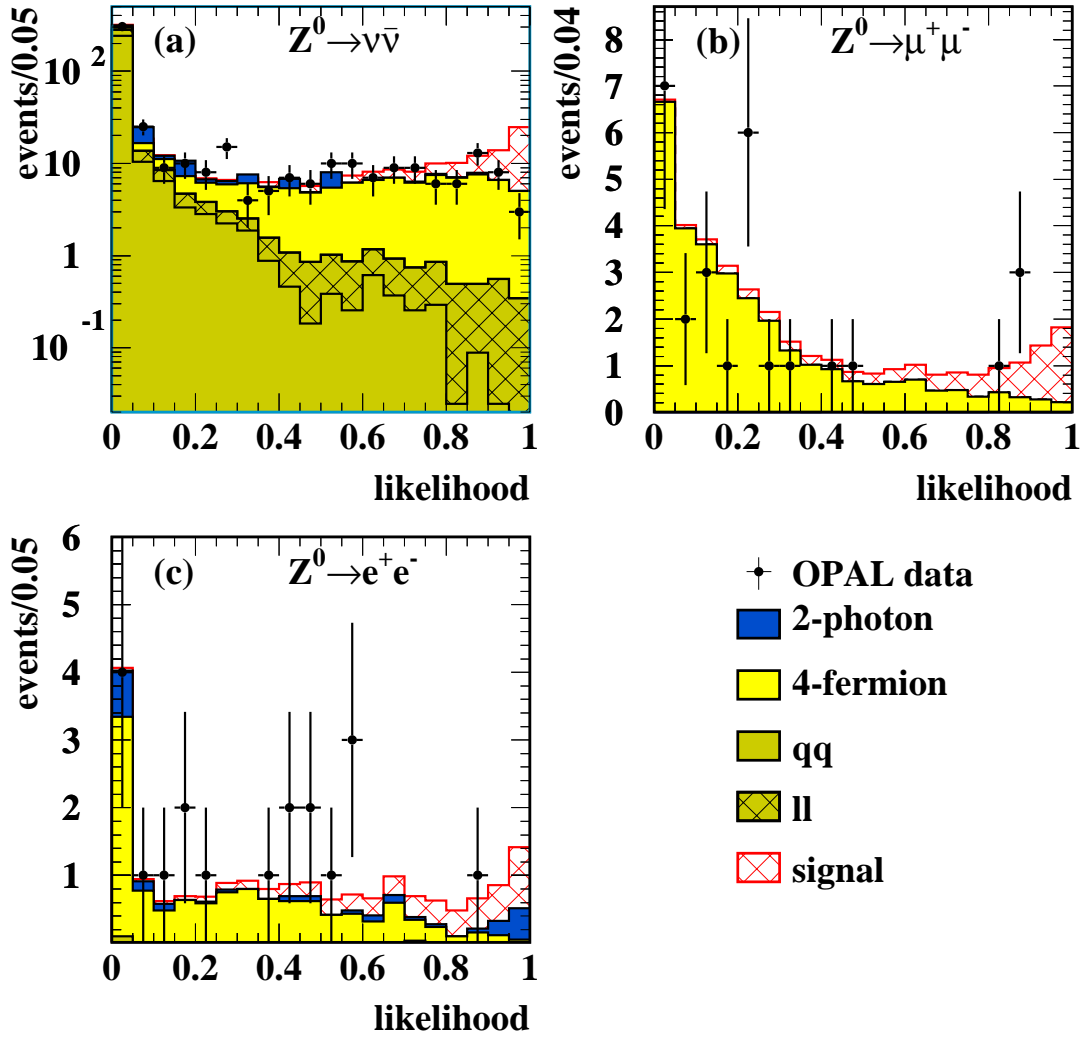
Figure 5: *The likelihood distribution functions in the (a)* $Z^0 \to \nu\bar{\nu}$ *(b)* $Z^0 \to \mu^+\mu^-$ *and (c)* $Z^0 \to e^+e^-$ *channels are shown for the data, the Standard Model backgrounds and the reference signal (the mixture of all signal hypotheses) for* E_{CM}=189–209 GeV *combined. The backgrounds are added and normalised to the data integrated luminosity.*
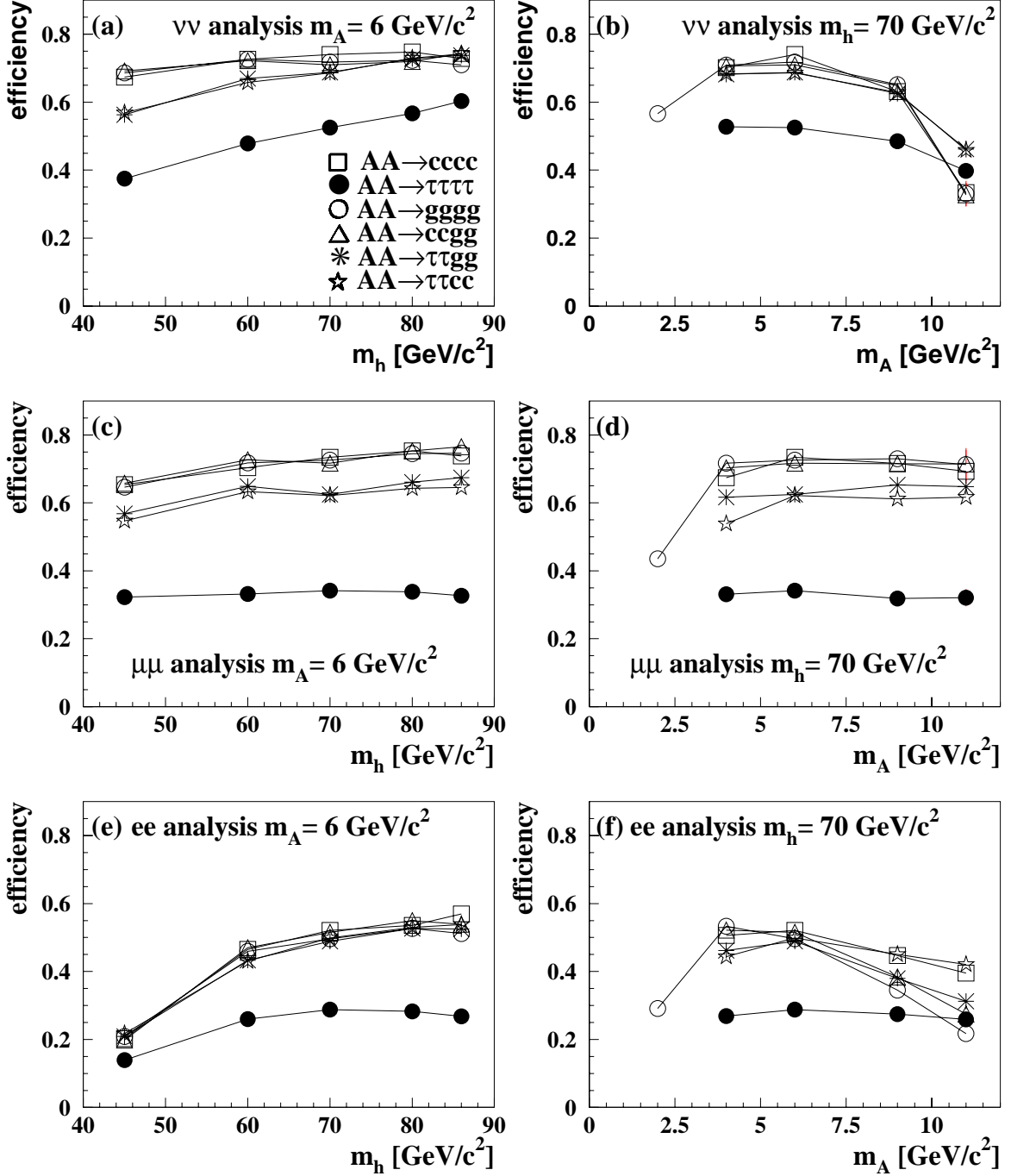
Figure 6: *Signal selection efficiencies at $E_{CM} = 189$ GeV versus $m_h(m_A)$ for $m_A = 6$ GeV/c^2 ($m_h = 70$ GeV/c^2) for the missing energy and the leptonic channels. The efficiencies are shown without any cut on the likelihood variable for all six decay channels of a $A^0 A^0$ pair with A^0 decaying into $c\bar{c}$, $\tau^+\tau^-$ or gg.*
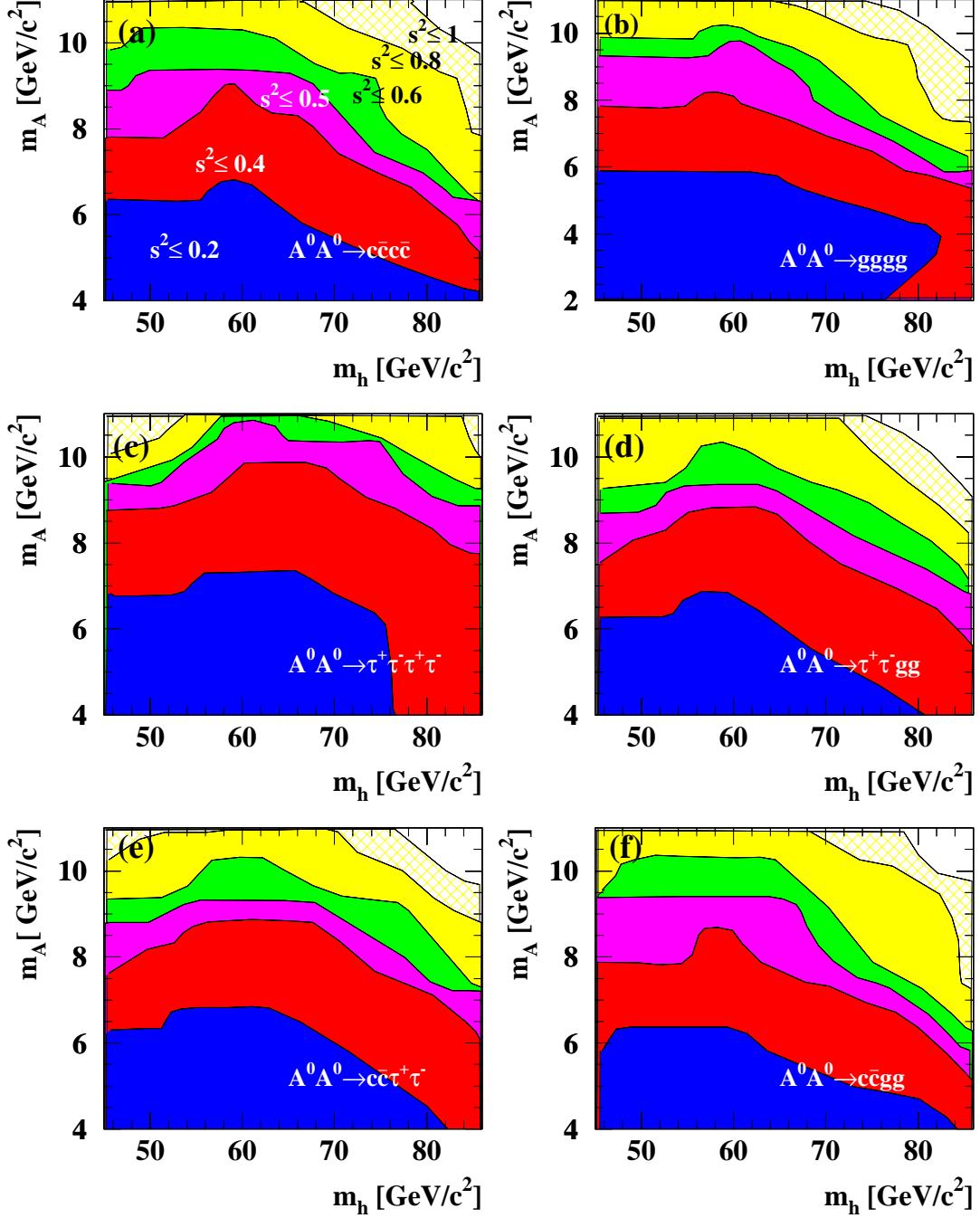
OPAL

Figure 7: *Upper limits at 95% CL for s^2 in the m_A versus m_h plane, assuming 100% decays of h^0 into A^0A^0 and 100% decays of A^0A^0 into (a) $c\bar{c}c\bar{c}$ (b) gggg (c) $\tau^+\tau^-\tau^+\tau^-$ (d) $\tau^+\tau^-$gg (e) $c\bar{c}\tau^+\tau^-$ and (f) $c\bar{c}$gg. The iso-contour lines are for values of $s^2 \leq 1$, 0.8, 0.6, 0.5 , 0.4 and 0.2. These limits are derived using the combined results from $Z^0 \to \nu\bar{\nu}$, $Z^0 \to \mu^+\mu^-$ and $Z^0 \to e^+e^-$ channels and for centre-of-mass energies between 189 and 209 GeV.*

25

Figure 8: *Expected (dashed contour) and observed (light grey area) excluded regions at 95% CL in the m_A versus m_h plane for the MSSM no-mixing benchmark scenario. These limits are derived using the combined results from $Z^0 \rightarrow \nu\bar{\nu}$, $Z^0 \rightarrow \mu^+\mu^-$ and $Z^0 \rightarrow e^+e^-$ chann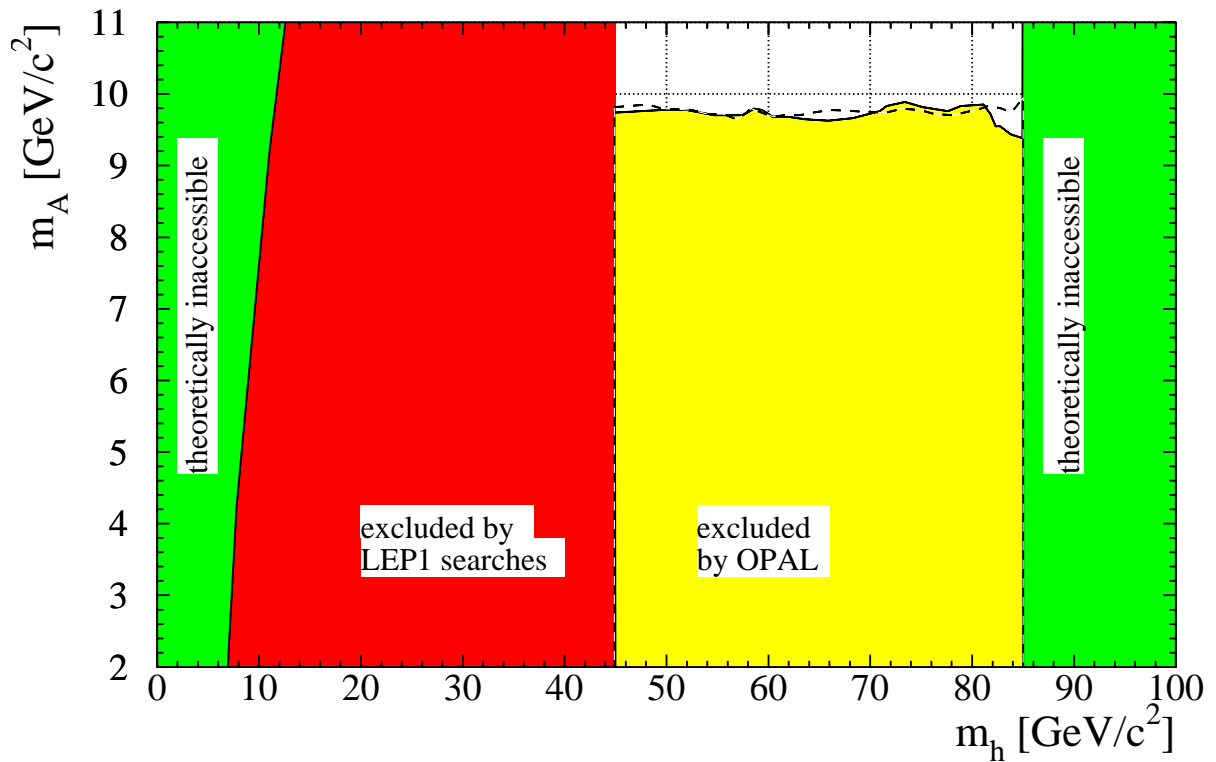els and for centre-of-mass energies between 189 and 209 GeV. The theoretically inaccessible regions and the region excluded by LEP 1 are also shown by darker areas.*